AIAA JOURNAL
Vol. 48, No. 1, January 2010

# Multi-Axial Fatigue-Life Prediction via a Strain-Energy Method

Onome Scott-Emuakpor,* Tommy George, and Charles Cross
*U.S. Air Force Research Laboratory, Wright-Patterson Air Force Base, Ohio 45433*
and
M.-H. Herman Shen
*The Ohio State University, Columbus, Ohio 43210*

DOI: 10.2514/1.39296

**A strain-energy-based method has been developed to predict the fatigue life of a structure subjected to either shear or biaxial bending loads at various stress ratios. The framework for this method is an advancement of previously conducted research that validates a uniaxial energy-based fatigue-life-prediction approach. The understanding behind the approach states that the total strain energy dissipated during a monotonic fracture and a cyclic process is the same material property, where the experimental strain-energy density of each can be determined by measuring the area underneath the monotonic true stress–strain curve and the area within a hysteresis loop, respectively. The developed framework consists of two elements: a life-prediction method that calculates shear fatigue-life cycles and a multi-axial life-prediction method capable of calculating biaxial fatigue-life cycles. A comparison was made between the two framework elements and experimental results from three different aluminum alloys. The comparison shows encouraging agreement, thus providing credence in the prediction capabilities of the proposed energy-based framework.**

## Nomenclature

| | | |
|---|---|---|
| $C$ | = | material parameter for cyclic strain |
| $C_s$ | = | material parameter for cyclic shear strain |
| $E$ | = | modulus of elasticity |
| $F$ | = | applied load |
| $G$ | = | shear modulus |
| $N$ | = | number of cycles to failure |
| $p$ | = | constant denoting principal direction of stress and strain |
| $R$ | = | alternating stress ratio (minimum versus maximum stress) |
| $R_y$ | = | distance from the neutral axis to the specimen surface |
| $U_T$ | = | multi-axial strain energy per surface area per cycle |
| $W_{\text{cycle}}$ | = | strain-energy density per cycle |
| $W_N$ | = | fatigue strain-energy density |
| $X, Y$ | = | coordinate axes |
| $\beta_1$ | = | monotonic stress regression slope |
| $\beta_2$ | = | monotonic stress regression constant |
| $\gamma$ | = | shear strain |
| $\gamma_{\text{cycle}}$ | = | cyclic shear strain |
| $\gamma_{\text{mean}}$ | = | shear mean strain |
| $\gamma_u$ | = | ultimate shear strain |
| $\gamma_0$ | = | material parameter for monotonic shear strain |
| $\varepsilon$ | = | strain |
| $\varepsilon_a, \varepsilon_b, \varepsilon_c$ | = | directional strain for a 60 deg rosette |
| $\varepsilon_{\text{cycle}}$ | = | peak-to-peak cyclic strain |
| $\varepsilon_f$ | = | failure strain |
| $\varepsilon_n$ | = | ultimate tensile strain |
| $\varepsilon_o$ | = | material parameter for monotonic strain |
| $\varepsilon_1, \varepsilon_2, \varepsilon_3$ | = | principal strain |
| $\nu$ | = | Poisson's ratio |
| $\sigma$ | = | stress |
| $\sigma_E$ | = | new equivalent stress value for nonlinear load analysis |
| $\sigma_{\text{PP}}$ | = | peak-to-peak cyclic stress |
| $\sigma_c$ | = | material parameter for cyclic strain |
| $\sigma_{\text{equiv}}$ | = | equivalent stress |
| $\sigma_{\text{max}}$ | = | maximum alternating stress |
| $\sigma_{\text{min}}$ | = | minimum alternating stress |
| $\sigma_n$ | = | ultimate tensile stress |
| $\sigma_o$ | = | material parameter for monotonic strain |
| $\sigma_p$ | = | general form for principal stress |
| $\sigma_1, \sigma_2, \sigma_3$ | = | principal stress |
| $\tau$ | = | shear stress |
| $\tau_{\text{PP}}$ | = | peak-to-peak shear stress |
| $\tau_c$ | = | material parameter for cyclic shear strain |
| $\tau_{\text{mean}}$ | = | mean shear stress |
| $\tau_o$ | = | material parameter for monotonic shear strain |
| $\tau_u$ | = | ultimate shear stress |
| $\tau_y$ | = | 0.2% shear yield stress |

Received 23 June 2008; accepted for publication 10 September 2009. 

*Onome.Scott-Emuakpor@wpafb.af.mil (Corresponding Author).

## I. Introduction

STRUCTURAL components in gas turbine engines are often designed to be failure-free throughout significant durations. To ensure this, fatigue design tools such as a stress-versus-cycles plot (S–N curve) have been used to observe fatigue strength due to the respective failure cycles. Other tools for assessing fatigue properties are the Goodman diagram and the modified Goodman diagram [1]. The Goodman diagram is a plot of alternating stress vs mean stress and represents the fatigue properties of a material at a specified number of failure cycles. The Goodman diagram and the S–N curve are often constructed with uniaxial fatigue data, which is conventionally acquired by servohydraulic machinery operating in tension/compression (axial). High-cycle fatigue (HCF) of turbine engine blades, however, often occurs under high-order bending or combined bending and twist modes [2]. Therefore, the uniaxial fatigue results from the Goodman diagram and the S–N curve are insufficient means for characterizing the fatigue that occurs in gas turbine engine blades. Adding to this insufficiency, conventional

uniaxial fatigue testing requires a significant amount of time to obtain a single HCF result, due to operating frequencies in the order range of 10–100 Hz. This means that an extremely long time is required to construct several data points on a HCF Goodman diagram.

To generate experimental data that provided a realistic comparison to turbine engine blade fatigue life, a vibration-based testing method was developed to acquire uniaxial bending fatigue results [2,3]. The test method is carried out by supplying a dynamic base excitation from an electrodynamic shaker to a cantilever specimen at a specified high resonant frequency, roughly between 1200–1600 Hz, that shows free-edge bending behavior [2,3]. This methodology, along with a prestraining procedure [4], is also capable of acquire fatigue for various stress ratios. Therefore, the vibration-based testing method has the capability to construct a uniaxial bending Goodman diagram [4,5]. Because of the operational frequency of the vibration-based testing device, which is significantly higher than conventional tension/compression devices, Goodman fatigue data can be constructed within a reasonable time frame. In other words, the use of the vibration-based method requires only 1.5 to 2.5 h to accumulate $10^7$ cycles, as opposed to more than 28 h for the conventional method.

Along with experimentally representing the uniaxial bending behavior of gas turbine engine components at high resonant frequencies, developing a design tool to observe multi-axial fatigue was essential as well. This led to understanding the connection between strain energy and failure. This relationship has been studied since the earlier part of the 20th century [6]. In the 1940s and 1950s, a number of well-publicized attempts to relate strain energy per cycle to the number of cycles for failure were considered and resulted in minimal success [7]. Success in this area was achieved by introducing the hypothesis stating that under cyclic loading there exists a critical energy value at which failure occurs [8]. Further investigation of this assumption led to the introduction of a more sufficient correlation between the fatigue life of a material and the strain-energy dissipation during the fatigue process. The introduced correlation states that the strain energy required to fracture a material monotonically is the same as the strain energy accumulated during a cyclic fatigue procedure [7,9]. Therefore, the critical energy value for each material is the monotonic strain energy. Based on this understanding, an energy-based fatigue-life-prediction method with the capability of accurately predicting uniaxial fatigue life (bending and tension/compression) at various stress ratios was developed [10,11].

The development of an energy-based multi-axial fatigue-life-prediction method is presented in this paper. Also presented is an energy-based shear fatigue-life-prediction method. Both the shear and the multi-axial prediction methods were compared with aluminum-alloy experimental results. The comparisons show encouraging correlation and promise for the entire energy-based fatigue-life-prediction criterion.

## II. Previous Research Scope

### A. Improved Energy-Based Prediction Method for Tension/Compression

Though several energy-based methods for predicting tension/compression fatigue life have been developed [7,9], an improved criterion with the capability to also predict uniaxial bending fatigue life was essential. This improved energy-based criterion was developed from the stress–strain representation of the monotonic and cyclic loading behavior displayed in Eqs. (1–3). Equations (1) and (2) represent the respective stress–strain relation before and after the necking phenomenon, and Eq. (3) is the stress–strain relation used to construct one cyclic (hysteresis) loop [9,10]. The relationship of Eq. (3) was developed based on the observation of cyclic stress and strain on a generalized coordinate system. This coordinate system, which can be seen in Fig. 1, plots the minimum stress–strain point of the hysteresis loop as the origin:

$$\varepsilon = \frac{\sigma}{E} + \varepsilon_o \sinh\left(\frac{\sigma}{\sigma_o}\right) \tag{1}$$

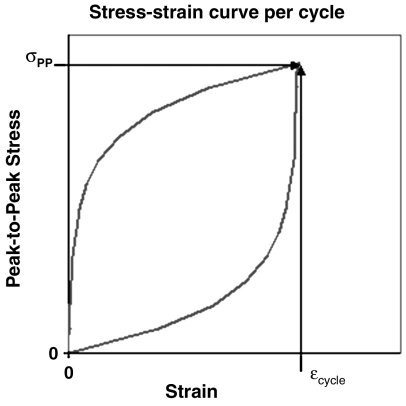


**Fig. 1 Generalized hysteresis loop.**

$$\sigma = \beta_1 \varepsilon + \beta_o \tag{2}$$

$$\varepsilon_{\text{cycle}} = \frac{\sigma_{\text{PP}}}{E} + \frac{1}{C}\sinh\left(\frac{\sigma_{\text{PP}}}{\sigma_c}\right) \tag{3}$$

The parameters for Eqs. (1–3) are defined as follows: $\sigma$ is the value for stress at the surface of the specimen; $\varepsilon$ is the strain corresponding to the stress $\sigma$; $\beta_1$ and $\beta_o$ are the respective slope and intercept of the stress–strain relationship in the region from ultimate tensile to fracture (necking region); $\sigma_{\text{pp}}$ is the generalized stress value corresponding to the generalized cyclic strain $\varepsilon_{\text{cycle}}$ [$2\sigma$ is substituted for $\sigma_{\text{pp}}$ in Eq. (3) after all necessary derivations]; $E$ is the modulus of elasticity, and the variables $\sigma_c$, $\sigma_o$, $\varepsilon_o$, and $C$ are curve-fit parameters [10]. The curve-fit parameters for the cyclic and monotonic representations are statistically acquired by comparing the respective Eqs. (1–3) with experimental low-cycle and monotonic-tensile experimental results [10,12].

The energy-based prediction method calculates fatigue life by taking the total monotonic strain-energy density and dividing it by the strain-energy density for one cycle. The total strain-energy density dissipated during a monotonic process is determined as the area underneath the curve constructed by Eqs. (1) and (2). The strain-energy density for one cycle, however, is calculated based on two assumptions: the generalized coordinate system of Fig. 1 is used, and the tensile behavior of the hysteresis loop is the same as the compressive behavior. Therefore, cyclic strain-energy density is defined by Eq. (4) and the tension/compression fatigue life of a specified stress amplitude level $\sigma$ is calculated by Eq. (5) [10]. In Eq. (5), $\sigma_n$ is the ultimate stress, $\varepsilon_f$ is the fracture strain, and $\varepsilon_n$ is the ultimate strain:

$$W_{\text{cycle}} = \sigma_{\text{PP}}\varepsilon_{\text{cycle}} - 2\int_0^{\sigma_{\text{PP}}} \varepsilon_{\text{cycle}}\, \mathrm{d}\sigma_{\text{PP}} \tag{4}$$

$$N = C\frac{\sigma_n(\varepsilon_n - \frac{\sigma_n}{2E}) - \varepsilon_o\sigma_o[\cosh(\frac{\sigma_n}{\sigma_o}) - 1] + \frac{\beta_1}{2}(\varepsilon_f^2 - \varepsilon_n^2) + \beta_o(\varepsilon_f - \varepsilon_n)}{2\sigma_c\{\frac{\sigma}{\sigma_c}\sinh(\frac{2\sigma}{\sigma_c}) - [\cosh(\frac{2\sigma}{\sigma_c}) - 1]\}} \tag{5}$$

The results from Eq. (5) are compared with previously acquired fully reversed tension/compression Al 6061-T6 experimental results and the corresponding linear regression curve on the S-N plot of Fig. 2. The comparison shows that the criterion provides good life estimations for tension/compression fatigue results. To further validate the accuracy of the comparison, experimental strain-energy density per cycle is plotted with the corresponding cycles to failure. These results are then compared with the energy-based predicted cyclic strain-energy density and the related cycles to failure in Fig. 3. It has been previously presented that the logarithmic slope of this comparison is roughly −0.6 [13]. Though the experimental results of

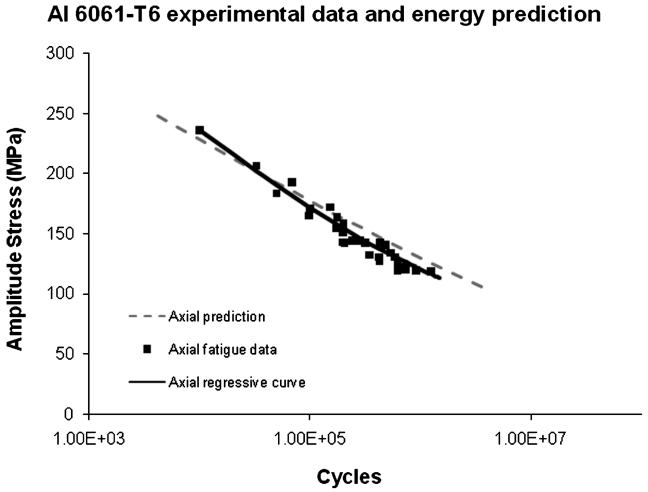


**Fig. 2 Fully reversed tension/compression fatigue-life comparison for Al 6061-T6 [10].**

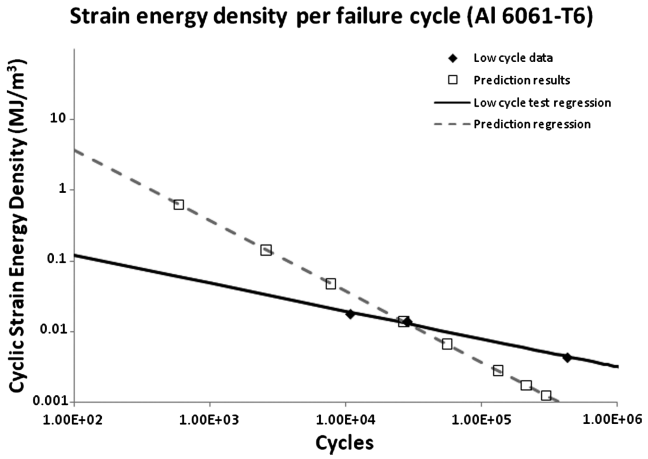


**Fig. 3 Fully reversed tension/compression cyclic strain-energy comparison for Al 6061-T6 [11].**

Fig. 3 agree with this belief, further analysis of the cyclic strain-energy density calculation method is conducted to provide reasoning for this agreement. Conclusion of this analysis shows that the variation between experimental and analytical results is more obvious in test data with a higher standard deviation of the curve fit between Eq. (3) and the experimental hysteresis loop. Because of a more sensitive stress–strain comparison, a minor deviation of the curve fit causes major variation in strain-energy density calculation. Therefore, the cyclic curve-fit parameters that provided minimal standard deviation were used in the prediction method of Eq. (5).

### B. Improved Energy-Based Prediction Method with Stress Gradient Effect (Bending)

To extend the tension/compression energy-based criterion to the bending case, the difference between stress gradient effect through the thickness of the bending and tension/compression specimen was evaluated. This difference is illustrated in Fig. 4. Since the stress distribution of the bending specimen varies with respect to the distance from the neutral axis, the strain energy through the thickness of each bending fatigue specimen (effective strain energy) was evaluated. To determine effective strain energy, the alternating stress from the monotonic and cyclic strain equations was written as a function of the vertical axis [11]. Bending fatigue-life-prediction results were calculated from the energy-based method of Eq. (6), which is the monotonic strain energy per surface area divided by the cyclic strain energy per surface area:

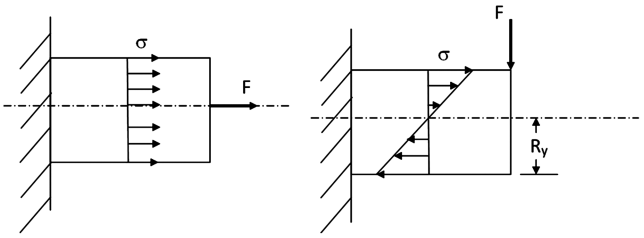


**Fig. 4 Stress distribution of uniaxial specimens.**

$$N = \frac{C\,\dfrac{\sigma_n(\varepsilon_n - \frac{\sigma_n}{2E}) - \varepsilon_o\sigma_o[\cosh(\frac{\sigma_n}{\sigma_o}) - 1] + \frac{\beta_1}{2}(\varepsilon_f^2 - \varepsilon_n^2) + \beta_o(\varepsilon_f - \varepsilon_n)}{\sigma_c[\cosh(\frac{2\sigma}{\sigma_c}) - \frac{3\sigma_c}{2\sigma}\sinh(\frac{2\sigma}{\sigma_c}) + 2]} \tag{6}$$

A prediction-versus-experiment comparison is shown in Fig. 5 for both uniaxial cases of Al 6061-T6.

### C. Improved Energy-Based Method with Mean Stress Effect

When positive mean stress is included in a fatigue procedure, the cycles required for fatigue are reduced because strain-energy density is dissipated monotonically and plastic strain per cycle is increased [11]. The total strain-energy density required for fatigue at stress ratio

$$(R = \sigma_{\min}/\sigma_{\max}) \geq -1.0$$

is acquired by subtracting the monotonic strain-energy density dissipated by mean stress from the total strain-energy density during monotonic fracture [11]. Determining the strain-energy density per cycle, however, requires a clear understanding of cyclic behavior with mean stress effect. When evaluating the fully reversed tension/compression cyclic behavior, two assumptions were set in place: the strain equation was determined from a generalized coordinate system, and the compressive portion of the cyclic stress–strain relation is the same as to the tensile [10]. Both of these statements are also assumed for cyclic loading with mean stress effect. Therefore, Eq. (3) and all the corresponding parameter values are still used to characterize the stress–strain behavior. The difference between the fully reversed hysteresis loop and the hysteresis loop with mean stress effect can be seen in the Al 6061-T6 experimental results of Fig. 6. The figure shows that the compressive curve does not connect to construct a complete loop when a mean stress is present. It is therefore assumed that the initial and final points per cycle are located on the horizontal mean stress line of the generalized coordinate system. These changes are applied to the tension/compression calculation method of Eq. (5). Comparisons between tension/compression experimental results and energy-based prediction are

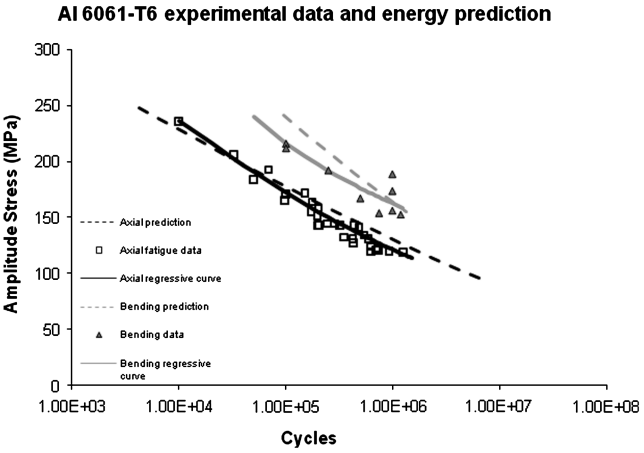


**Fig. 5 Fully reversed uniaxial fatigue-life comparison (bending and tension/compression) [11].**

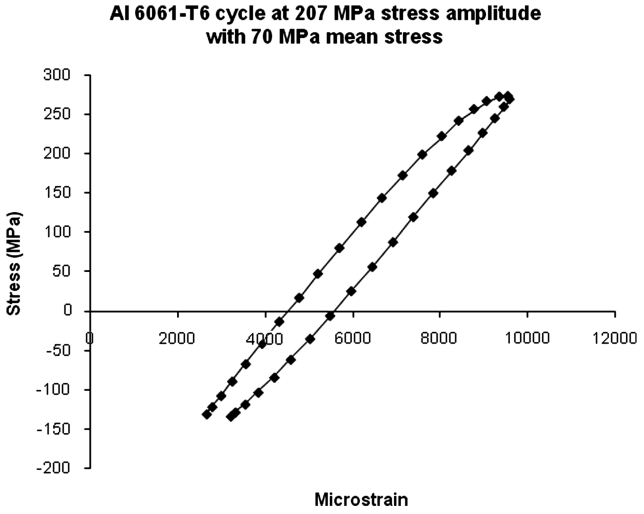


**Fig. 6 Experimental hysteresis loop with mean stress [11].**

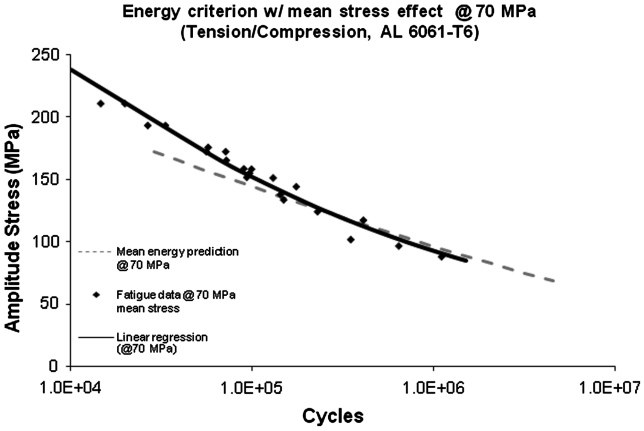


**Fig. 7 Tension/compression fatigue-life comparison with 70 MPa mean stress effect [11].**

shown in Figs. 7 and 8 for mean stress values of 70 and 138 MPa, respectively.

## III. Experimental Procedures

### A. Shear-Testing Procedures

Three types of experimental tests were conducted using the shear-loading procedure: fatigue, monotonic fracture, and low-cycle testing. All three shear experiments were conducted using the ASTM

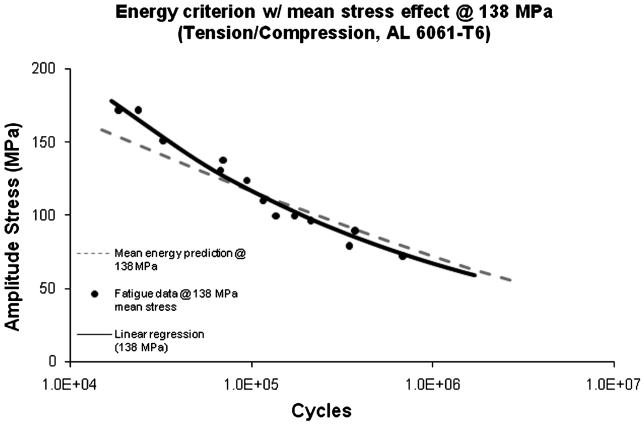


**Fig. 8 Tension/compression fatigue-life comparison with 138 MPa mean stress effect [11].**

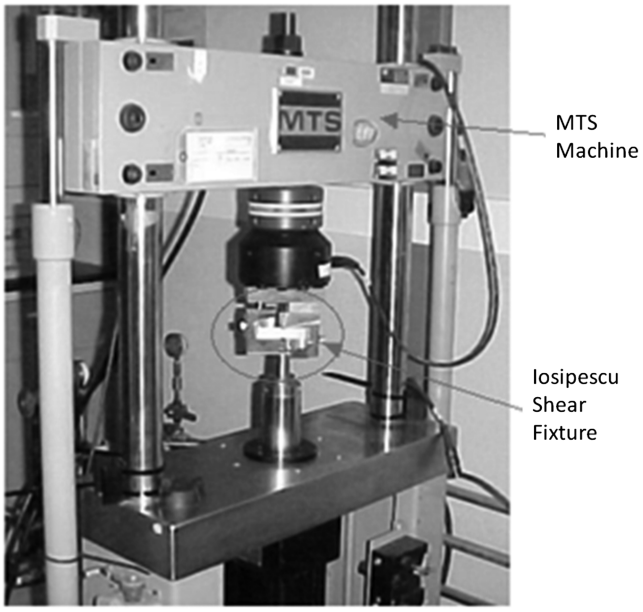


**Fig. 9 MTS with Iosipescu fixture and setup.**

D5379 [14] standard for composites and polymers, which suggests the Iosipescu testing fixture shown in Fig. 9. The recommended specimen under shear is a V-notched flat strip coupon that is referenced by the ASTM D5379 [14] standard and shown in Fig. 10. Based on an offset/eccentric load, the thickness is desired to be 0.635 mm to prevent a moment about the horizontal axis. The pure shear load is distributed to the V-notched specimen using the MTS System Corporation machine shown in Fig. 9. The entire shear test setup is located in the Turbine Engine Fatigue Facility (TEFF) of the U.S. Air Force Research Laboratory in the Propulsion Directorate at Wright-Patterson Air Force Base .

The two strain gauges used to measure shear strain were micro-measurement models CEA-13-062WT-350 and EP-08-125AC-350. Each gauge read normal strain at $\pm 45$ deg from the horizontal axis of the test specimen. Shear strain was acquired by subtracting normal strain results of the $-45$ deg gauge from the results of the $+45$ deg strain gauge [14]. This form of measurement was used to acquire strain for the low cycle and the monotonic testing procedures only. Experimental results required for fatigue tests were the load, cycles, and stroke (initial and final absolute displacement positions). These results were acquired with the TestStarIIs data acquisition system of the MTS machine.

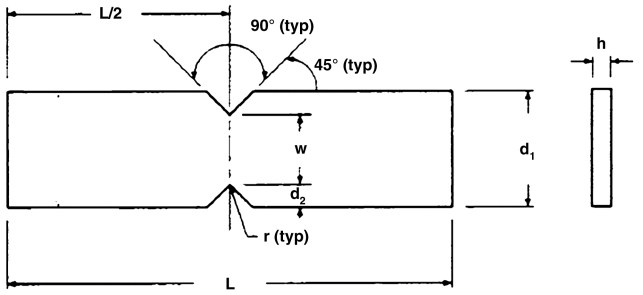


Nominal Specimen Dimensions

| | | |
|---|---|---|
| $d_1$ | = | 20.0 mm [0.75 in.] |
| $d_2$ | = | 4.0 mm [0.15 in.] |
| h | = | as required |
| L | = | 76.0 mm [3.0 in.] |
| r | = | 1.3 mm [0.05 in.] |
| w | = | 12.0 mm [0.45 in.] |

**Fig. 10 ASTM D5379 [14] V-notched beam specimen.**

Like the vibration-based bending case, fatigue during shear experimentation is defined as the instance a crack appears on the tested specimen. A crack is detected by observing the inconsistency of cyclic experimental results. Inconsistency in the shear fatigue experiment can be seen in an analysis of relative displacement position versus number of cycles. The belief behind the analysis states that when a crack is formed in the specimen, the stiffness decreases. Since the shear fatigue testing is controlled by load amplitude, a larger displacement is required as a crack propagates. Therefore, based on the reverse polarity of the TestStarIIs, the initial stroke displacement value begins to nonlinearly decrease when a crack forms in the specimen. This behavior can be seen in Fig. 11.

Crack initiation and complete fracture in tension/compression HCF cases have a negligible difference in cycle count [15]. Therefore, in order to correlate the failure from the monotonic-tensile and cyclic tension/compression procedures, monotonic failure is defined as the point of complete fracture. This application, however, is not valid for the shear case. Crack initiation and complete fracture occur at noticeably different cycles. This difference can be seen on the shear fatigue data of Fig. 11. Based on this understanding, monotonic shear failure is observed at the point of crack initiation. Monotonic crack initiation can be determined from the load versus displacement plot in Fig. 12. The figure shows a sharp and distinct decrease in the applied load, which is based on the change in the specimen's stiffness when a crack has developed.

### B. Biaxial Fatigue-Testing Procedure

Biaxial fatigue results are acquired using the vibration-based testing method [2,3,16]. Stated previously in the Introduction, the vibration-based test is defined as a dynamic base excitation being supplied to a cantilever specimen at a specified high resonant frequency. The base excitation is supplied to the specimen with the

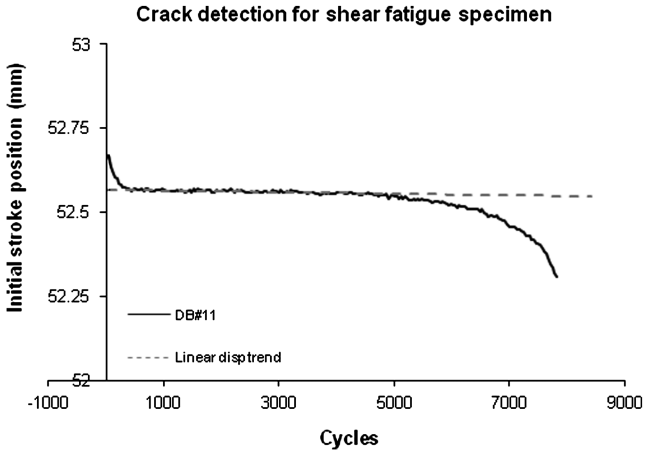


**Fig. 11 Relative specimen position at individual cycles.**

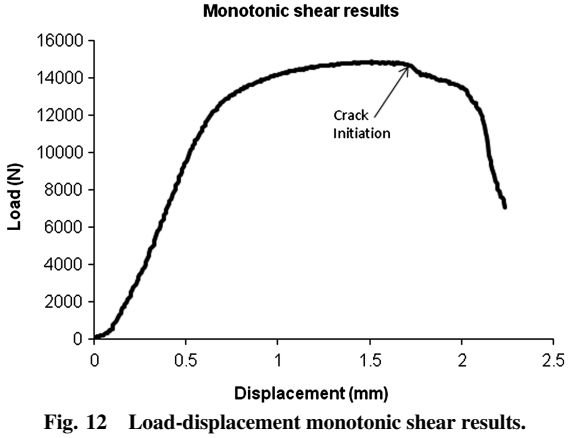


**Fig. 12 Load-displacement monotonic shear results.**

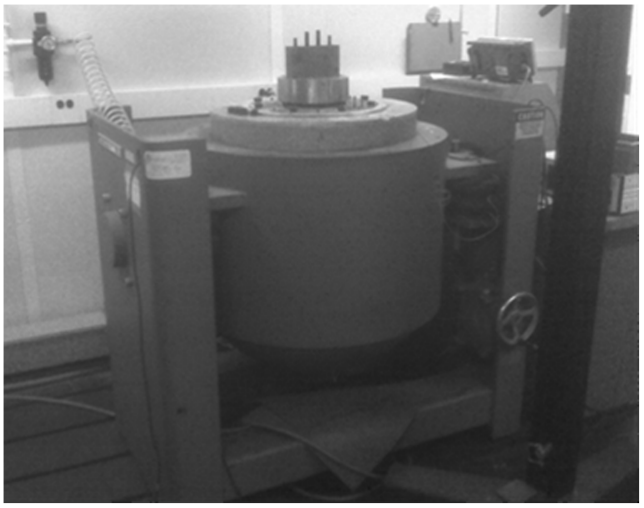

**Fig. 13 Ling 80 kN electrodynamic shaker.**

80 kN Ling electrodynamic shaker shown in Fig. 13. The biaxial vibration-based setup is located in the TEFF. This particular test has been successfully conducted in previous research [16].

The geometry for the biaxial specimen is shown in Fig. 14, in which 57.15 mm of the specimen is clamped. This specimen was developed via a geometrical design procedure discussed in [16] and was further optimized based on some constrained parameters from the original design [17]. The geometrical design procedure was conducted to provide a specimen with the capability of generating high excitation and a unique mode shape, which produced a more significant von Mises stress level at a region other than the clamped boundary and the edges of the test specimen. It is also desired that the geometrical design procedure should provide the best biaxial bending stress ratio for experimental fatigue. In other words, the $x$-to-$y$ stress ratio is 1.5.

Before conducting a biaxial fatigue test, a finite element method (FEM) harmonic analysis is carried out for three reasons: validate the geometrical optimization procedure, establish the location of the measurement instrumentation on each specimen, and determine the frequency at which biaxial bending occurs. This analysis is generated using two FEM software: ABAQUS for processing only and IDEAS for pre- and postprocessing [16]. Results from a previous FEM analysis of the biaxial specimen are shown in Fig. 15. In this figure, the von Mises results (Fig. 15b) show that the maximum stress level is considerably larger in a region away from the clamped edge. Also shown is that the corresponding normal stress ratio for $X$ versus $Y$ (Figs. 15c and 15d, respectively) is approximately 1.5. This means that the biaxial fatigue crack will propagate along the $Y$-axis.

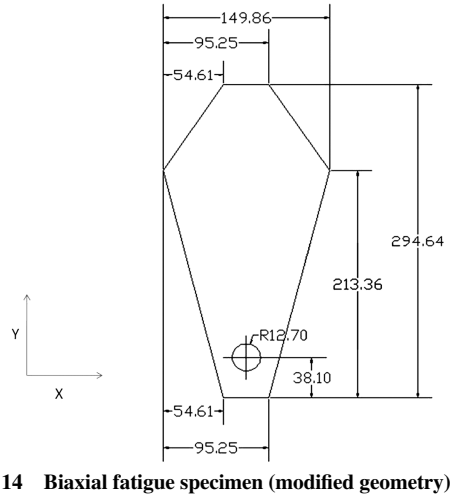


**Fig. 14 Biaxial fatigue specimen (modified geometry) [17].**

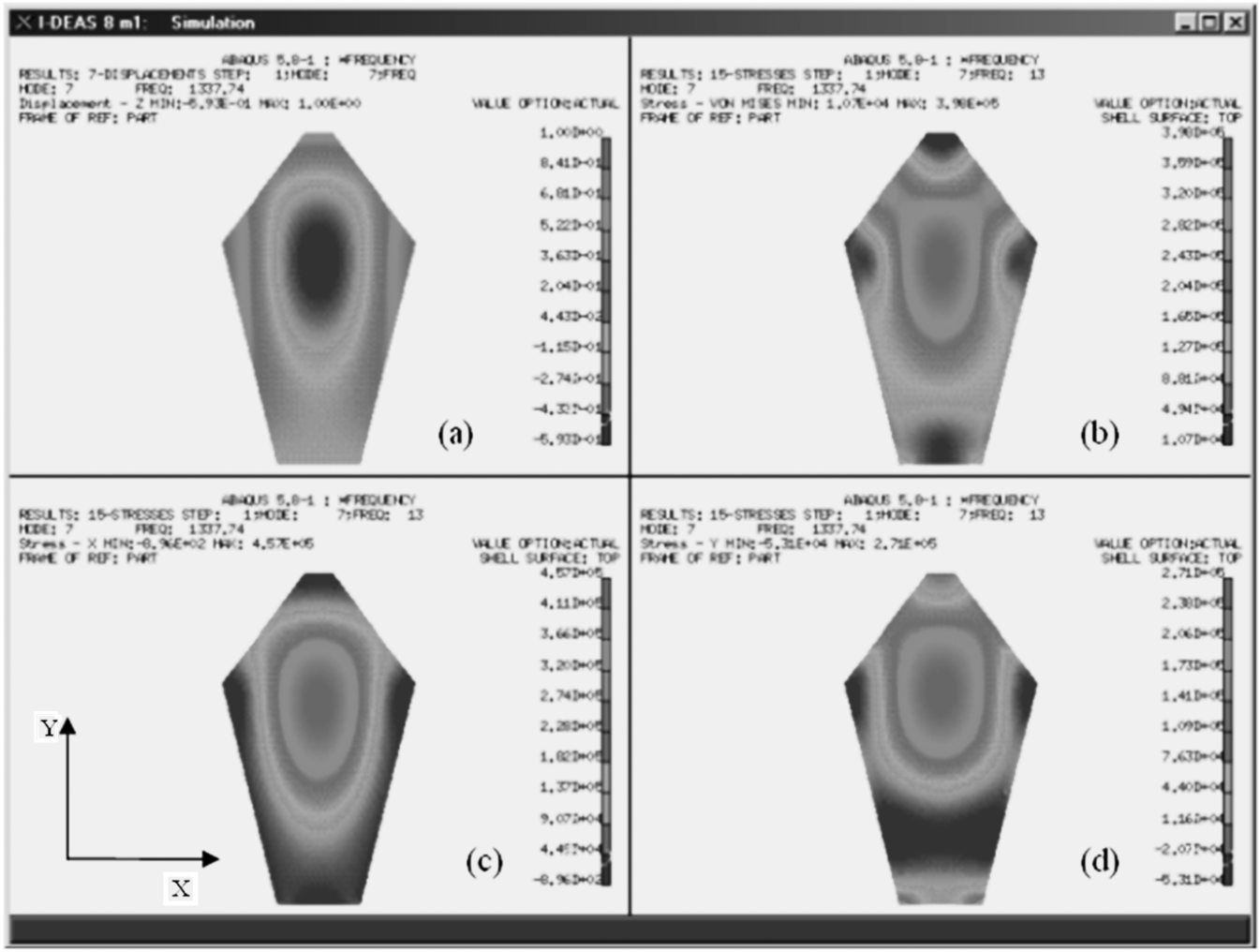


**Fig. 15 Biaxial FEM: a) mode shape, b) von Mises stress, c) *x*-direction stress, and d) *y*-direction stress.**

A laser vibrometer and a strain gauge are used to acquire velocity and strain results from biaxial experiments, respectively. The strain gauge used was a 60 deg rosette (SK-05-060WY-350), which is capable of reading normal strains in three directions. The rosette strain gauge has a limited fatigue-life rating. Therefore, the linear correlation in Fig. 16 was made between each of the rosette strain directions ($a$, $b$, and $c$) and the velocity data from the nonintrusive laser vibrometer. When cracks are present in biaxial specimens, they are detected by a rapid decrease in the single point velocity reading, which is due to a change in the specimen's stiffness.

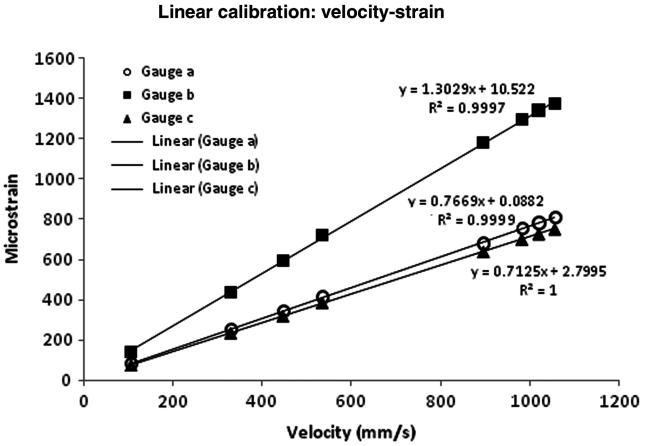


**Fig. 16 Linear calibration of the delta rosette strain gauge and the laser vibrometer.**

A valid assessment of biaxial fatigue strength requires the calculation of an equivalent stress. The von Mises stress calculation is used because the loading is fully reversed. To determine the von Mises stress, strain transformation relationship is used to calculate the principal strains from the rosette gauge results [18]. The principal strains are determined by Eq. (7), where the subscripts $a$, $b$, and $c$ represent strain in the three directions of the 60 deg rosette, and the numbers 1 and 3 represent the two principal strains due to 2-D strain transformation analysis. The principal stress corresponding to the principal strain can be determined by applying Hooke's law of general stress state [Eqs. (8–10)], where $\nu$ is Poisson's ratio and $E$ is the modulus of elasticity. Using the principal stress results, the von Mises stress is calculated with Eq. (11):

$$\varepsilon_{1,3} = \frac{\varepsilon_a + \varepsilon_b + \varepsilon_c}{3} \pm \frac{\sqrt{2}}{3}\sqrt{(\varepsilon_a - \varepsilon_b)^2 + (\varepsilon_b - \varepsilon_c)^2 + (\varepsilon_c - \varepsilon_a)^2} \tag{7}$$

$$\sigma_1 = \frac{E}{(1-\nu^2)}[\varepsilon_1 + \nu\varepsilon_3] \tag{8}$$

$$\sigma_2 = 0 \tag{9}$$

$$\sigma_3 = \frac{E}{(1-\nu^2)}[\varepsilon_3 + \nu\varepsilon_1] \tag{10}$$

$$\sigma_{\text{equiv}} = \sqrt{\frac{(\sigma_1 - \sigma_2)^2 + (\sigma_2 - \sigma_3)^2 + (\sigma_3 - \sigma_1)^2}{2}} \tag{11}$$

## IV. Experimental Results

### A. Monotonic Shear

Experimental data from an Al 6061-T6 monotonic shear test is shown in Fig. 17. These results were acquired with a square rosette strain gauge (CEA-13-062WT-350). Unfortunately the maximum elongation of this gauge, which is 3% strain, is rated for strains lower than the fracture shear strain of the tested specimen. To acquire strains up to the point of fracture, two individual large elongation gauges (EP-08-125AC-350) were used. The use of these gauges reduces the precision of the gauge placement. However, an agreeable comparison between the square rosette and the large elongation gauge was made in Fig. 18 to validate the precision of the application.

Equation (12) represents the monotonic shear stress–strain relationship. The parameters for this equation are defined the same way as the corresponding parameters used in the monotonic-tensile case [Eq. (1)]: $\tau$ is the shear stress level, $G$ is the shear modulus, and $\tau_o$ and $\gamma_o$ are curve-fit constants. The curve-fit constant $\tau_o$ is determined by Eq. (13), where $\tau_u$ is the applied stress of gauge failure, $\tau_y$ is the 0.2% yielding shear stress, and $\gamma_u$ is the shear strain at failure of the gauges. The parameter $\gamma_o$ is acquired by curve-fitting Eq. (12) to monotonic test results with a MATLAB optimization code [12]. The necessary parameters for Eqs. (12) and (13) are shown in Table 1.

$$\gamma = \frac{\tau}{G} + \gamma_o \sinh\left(\frac{\tau}{\tau_o}\right) \tag{12}$$

$$\tau_o = \frac{\tau_u - \tau_y}{\ell n(\gamma_u/0.002)} \tag{13}$$

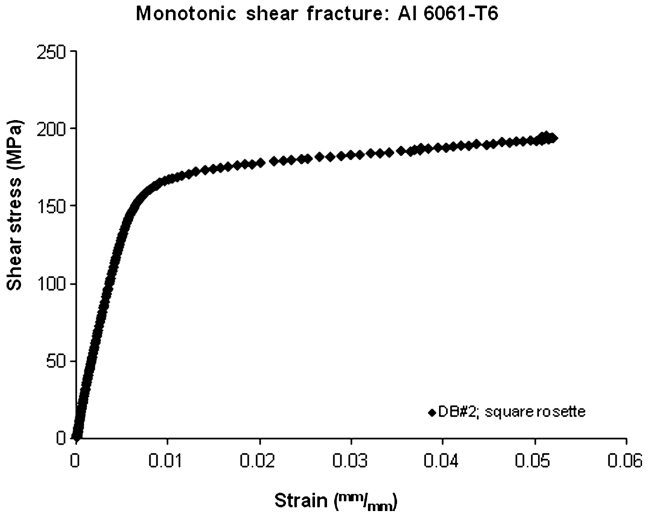


**Fig. 17 Monotonic shear stress–strain results.**

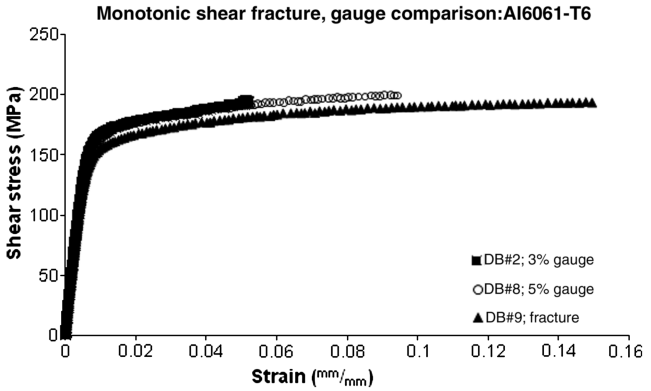


**Fig. 18 Monotonic comparison between three different gauge results.**

**Table 1 Material properties for shear strain approximation: Al 6061-T6**

| | |
|---|---|
| $\tau_y$, MPa | 165.1 |
| $\tau_u$, MPa | 195.0 |
| $\gamma_u$, mm/mm | 0.034205 |
| $\tau_o$, MPa | 10.6 |
| $\gamma_o$, mm/mm | 6.20E − 11 |

**Table 2 Computational results for cyclic stress–strain curve fit: Al 6061-T6**

| $\tau$, MPa | $\tau_{\text{mean}}$, MPa | Cycle no | $C_s$ | $\tau_c$, MPa | Std |
|---|---|---|---|---|---|
| 68.9 | 68.9 | 2 | 1.43E + 07 | 20.3 | 6.0859 |
| 82.7 | 0 | 2 | 1.00E + 05 | 64.8 | 2.2969 |
| 82.7 | 0 | 3 | 1.00E + 05 | 93.4 | 1.7009 |
| 96.5 | 0 | 1 | 1.00E + 05 | 50 | 2.4535 |
| 96.5 | 0 | 2 | 1.00E + 05 | 47.9 | 2.6532 |

### B. Low-Cycle Testing

Low-cycle Al 6061-T6 experimental data was curve-fit with the shear stress–strain representation of Eq. (14). In this equation, $C_s$, and $\tau_c$ are the curve-fit parameters and $\tau_{\text{pp}}$ is the generalized cyclic shear stress for the corresponding cyclic strain $\gamma_{\text{cycle}}$ ($\tau_{\text{pp}}$ is substituted by $2\tau$ after all derivations are completed). Like the tension/compression case, shear curve-fit parameters were acquired based on two assumptions: a generalized coordinate system is used, and tensile and compressive stress–strain behavior are the same. Following these assumptions, three low-cycle tests were conducted: two fully reversed and one with mean stress. Each test was conducted up to a cycle count of four. This cycle count is not at the value at which most materials reach stationary surface temperature during fatigue. However, Al 6061-T6 experiences minimal temperature change during cyclic loading [19]. Therefore, the low-cycle application conducted for shear analysis is acceptable. Similar to the tension/compression analysis of [10], Eq. (14) is curve-fit with each individual low-cycle case using a MATLAB optimization code [12]. The core of this code is the calculation of the standard deviation of the percent difference between Eq. (14) and the low-cycle experimental data. The results in Table 2 show that the fully reversed data at the third cycle of the 82.7 MPa load provide the best fit:

$$\gamma_{\text{cycle}} = \frac{\tau_{\text{pp}}}{G} + \frac{1}{C_s}\sinh\left(\frac{\tau_{\text{pp}}}{\tau_c}\right) \tag{14}$$

### C. Shear Fatigue Results

Based on the assembly of the Iosipescu fixture, some parts of the fixture are unable to handle large tensile loads for long durations. Therefore, all fatigue tests were conducted at $R = -10$. This means that the MTS machine and the test fixture stay in compression throughout the entire fatigue process. Since a shear load cannot be designated as compressive or tensile, however, the experimental fatigue mean loads were observed on a positive scale (i.e., $R = 0.1$) to simplify the fatigue-prediction manipulations. Shear fatigue results for Al 6061-T6, based on this positive loading scale, are shown in Fig. 19. To ensure accuracy in the test-fixture capability, experiments were conducted at frequencies between 10 and 15 Hz, which limited shear fatigue data in Fig. 19 to $10^5$ cycles.

### D. Uniaxial and Biaxial Test Results

Experimental fatigue-life data for uniaxial tension/compression and biaxial bending specimens were acquired from three different stocks of aluminum alloy. The exact alloys are unknown; however, experiments were conducted to attain the necessary mechanical properties of each material. The procedure for acquiring an axial fatigue-life-prediction method was followed for each aluminum-alloy stock [10]. Therefore, a few different uniaxial experimental results were required to develop the prediction method. First, numerous tensile tests were conducted to attain necessary mechanical

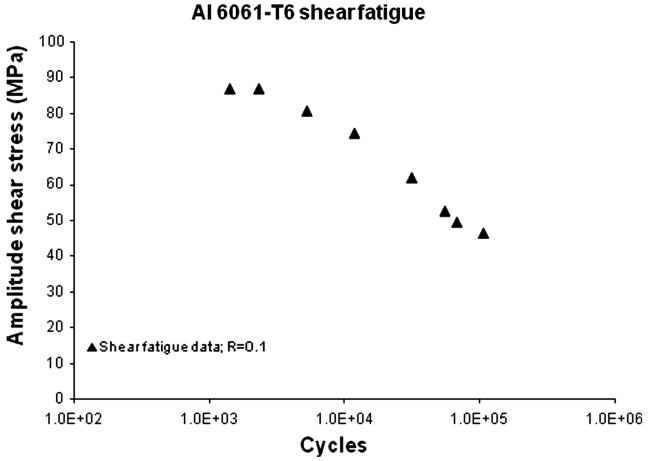


**Fig. 19 S–N data for shear loading.**

properties and energy results. Then tension/compression fatigue and low-cycle hysteresis test were conducted so the life-prediction method could be applied to each aluminum-alloy stock. The tension compression fatigue results are shown in Fig. 20.

Biaxial fatigue results were acquired from 11 specimens using a step-test method [20]. The method is conducted by cyclically loading a specimen at a specified number of cycles and at an alternating stress level much lower than anticipated fatigue stress. If failure does not occur by the end of the specified cycle count, the stress level is increase by a small fraction and the cyclic test is repeated. This entire process is continued until failure occurs. The results of the experimental biaxial fatigue tests are shown in Fig. 21.

## V. Shear-Energy-Based Fatigue Analysis

Energy-based fatigue-prediction analysis was developed based on the belief that the total strain energy required for monotonic failure is equivalent to the strain energy accumulated from cyclic failure. Because of this statement, a strain-energy density representation was developed for monotonic and hysteresis shear cases. Each strain-energy density representation is used to formulate the fully reversed energy-based shear fatigue-prediction criterion expressed by Eq. (15):

$$N = C_s \frac{\tau_u(\gamma_u - \frac{\tau_u}{2G}) - \gamma_o \tau_o[\cosh(\frac{\tau_u}{\tau_o}) - 1]}{2\tau_c\{\frac{\tau}{\tau_c}\sinh(\frac{2\tau}{\tau_c}) - [\cosh(\frac{2\tau}{\tau_c}) - 1]\}} \tag{15}$$

Since $R = 0.1$, mean stress effect was incorporated into the energy-based prediction analysis. Mentioned in Sec. II, there are two main effects in the prediction analysis caused by mean stress: strain-energy density is dissipated monotonically, and plastic deformation

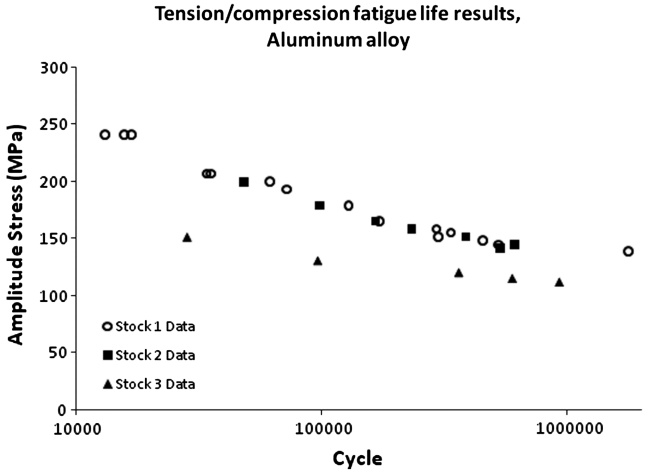


**Fig. 20 Fully reversed experimental tension/compression fatigue-life results.**

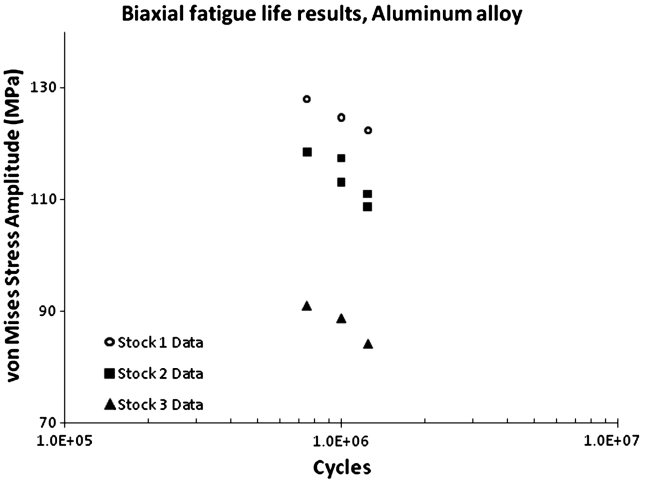


**Fig. 21 Experimental biaxial fatigue-life results.**

per cycle is increased. The mean shear stress $\tau_{\text{mean}}$ effects are applied to the monotonic and the fully reversed cyclic strain-energy density expressions used to construct Eq. (15). The resulting expressions are shown by Eqs. (16–20), where dividing Eq. (16) by Eq. (17) [Eq. (21)] predicts the number of failure cycles based on shear stress amplitude and a mean shear stress:

$$\begin{aligned} W_N = {} & \tau_u\left(\gamma_u - \frac{\tau_u}{2G}\right) + \gamma_o\tau_o\left[\cosh\left(\frac{\tau_u}{\tau_o}\right) - 1\right] \\ & - \left\{\tau_{\text{mean}}\left[\frac{\tau_{\text{mean}}}{G} + \gamma_o \sinh\left(\frac{\tau_{\text{mean}}}{\tau_o}\right)\right]\right. \\ & \left. + \gamma_o\tau_o\left[\cosh\left(\frac{\tau_{\text{mean}}}{\tau_o}\right) - 1\right]\right\} \end{aligned} \tag{16}$$

$$W_{\text{cycle}} = \tau_{\text{pp}}(\gamma_{\text{cycle}} + \gamma_{\text{mean}}) - \int_{\tau_{\text{mean}}}^{\tau_{\text{pp}}+\tau_{\text{mean}}} \gamma_{\text{cycle}}\,\mathrm{d}\tau_{\text{pp}} - \int_0^{\tau_{\text{pp}}} \gamma_{\text{cycle}}\,\mathrm{d}\tau_{\text{pp}} \tag{17}$$

$$\tau_{\text{pp}}(\gamma_{\text{cycle}} + \gamma_{\text{mean}}) = 2\tau\left[\frac{2\tau + \tau_{\text{mean}}}{G} + \frac{\sinh(\frac{2\tau+\tau_{\text{mean}}}{\tau_c})}{C_s}\right] \tag{18}$$

$$\begin{aligned} \int_{\tau_{\text{mean}}}^{\tau_{\text{pp}}+\tau_{\text{mean}}} \gamma_{\text{cycle}}\,\mathrm{d}\tau_{\text{pp}} = {} & \frac{1}{2GC_s}\tau_{\text{mean}}^2 C_s + 2\tau_c \cosh\left(\frac{\tau_{\text{mean}}}{\tau_c}\right)G \\ & - \frac{1}{2GC_s}(2\tau + \tau_{\text{mean}})^2 C_s - 2\tau_c \cosh\left(\frac{2\tau + \tau_{\text{mean}}}{\tau_c}\right)G \end{aligned} \tag{19}$$

$$\int_0^{\tau_{\text{pp}}} \gamma_{\text{cycle}}\,\mathrm{d}\tau_{\text{pp}} = \frac{-\tau_c G + 2\tau^2 C_s + \tau_c \cosh(\frac{2\tau}{\tau_c})G}{GC_s} \tag{20}$$

$$N = \frac{W_N}{W_{\text{cycle}}} \tag{21}$$

The energy-based fatigue-life-prediction method for the fully reversed and the $R = 0.1$ cases are successfully compared with shear experimental results in Fig. 22.

## VI. Multi-Axial Energy-Based Fatigue Analysis

To develop the energy-based multi-axial fatigue-life-prediction method, the general state of stress for an object in a monotonic and cyclic case was observed. Unlike the conventional state of stress analysis [21], the strain-energy functions are nonlinear. Critical strain energy is a constant scalar, and it is thus the monotonic strain energy. The effective strain energy per cycle, however, is acquired with the summation of effective strain energy (strain energy per surface area) for the six stress components acting on a general structure, which is

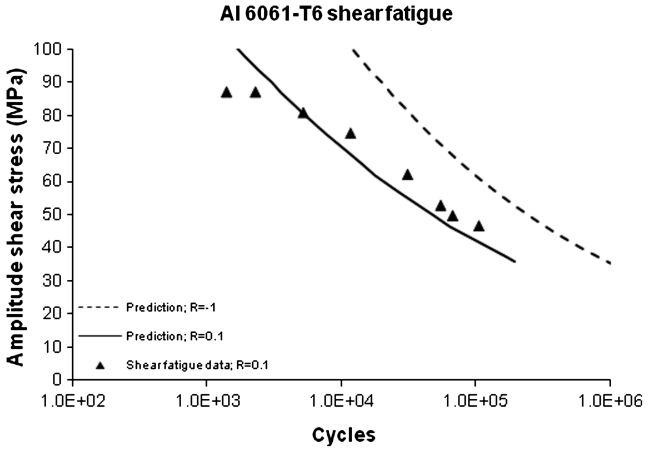


**Fig. 22 S–N comparison between predicted and experimental shear fatigue.**

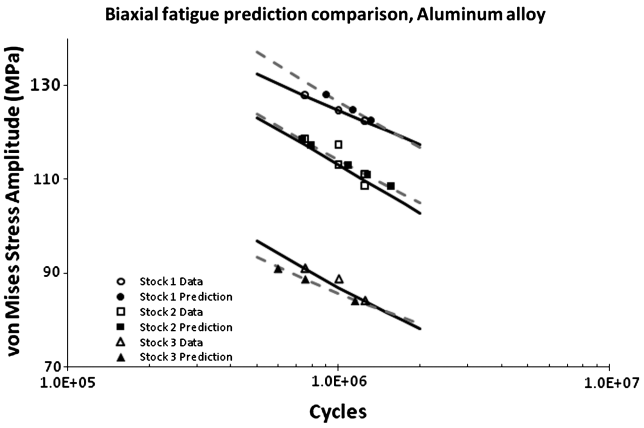


**Fig. 23 Biaxial experimental-prediction comparison for aluminum alloys.**

expressed by Eq. (22). This equation is made up of two terms: the effective strain-energy summation based on the shear stresses (i.e., $\tau$ is equal to $\tau_{xy}$, $\tau_{yz}$, or $\tau_{zx}$), and the effective strain-energy summation based on the normal stresses (i.e., $\sigma$ is equal to $\sigma_x$, $\sigma_y$, or $\sigma_z$). The variable $R_y$ in Eq. (22) denotes the distance from the neutral axis of the specimen. The effect of Poisson's ratio was neglected in the summation of the normal stresses. Poisson's ratio phenomenon on strain is determined by the deformation of the cross-sectional area of an object that is subjected to an applied load. Since high-cycle multi-axial fatigue operates at stress levels well within the elastic region of most metallic alloys, the cross-sectional deformation experienced during high-cycle multi-axial fatigue is minimal. Therefore, the exemption of Poisson's ratio from Eq. (22) should have minimal effect as well:

$$U_T = \sum \frac{4\tau_c}{C_s}\left\{\frac{\tau}{\tau_c}\sinh\left(\frac{2\tau}{\tau_c}\right) - \left[\cosh\left(\frac{2\tau}{\tau_c}\right) - 1\right]\right\}R_y + \sum \begin{cases} \frac{4\sigma_c}{C}\left\{\frac{\sigma}{\sigma_c}\sinh\left(\frac{2\sigma}{\sigma_c}\right) - \left[\cosh\left(\frac{2\sigma}{\sigma_c}\right) - 1\right]\right\}R_y, & \text{for tension/compression} \\ \frac{2\sigma_c}{C}\left[\cosh\left(\frac{2\sigma}{\sigma_c}\right) - \frac{3\sigma}{2\sigma_c}\sinh\left(\frac{2\sigma}{\sigma_c}\right) + 2\right]R_y, & \text{for bending} \end{cases} \tag{22}$$

Equation (22) is generally used to determine effective strain energy per cycle during multi-axial fatigue prediction. However, principal stresses can be used if the uniaxial loading mechanism is the same in the normal Cartesian directions ($x$, $y$, and $z$). By applying the principal stress laws, the multi-axial strain-energy density per cycle can be expressed by Eq. (23), where the subscript $p$ denotes the principle direction effective strain-energy expression being added in the summation. Multi-axial fatigue-life-prediction for biaxial loaded specimens is conducted by dividing the critical effective strain energy by Eq. (23). This prediction is compared, with promising results, to biaxial experimental data in Fig. 23:

$$U_T = \sum_{p=1}^{3} \begin{cases} \frac{4\sigma_c}{C}\left\{\frac{\sigma_p}{\sigma_c}\sinh\left(\frac{2\sigma_p}{\sigma_c}\right) - \left[\cosh\left(\frac{2\sigma_p}{\sigma_c}\right) - 1\right]\right\}R_y, & \text{for tension/compression} \\ \frac{2\sigma_c}{C}\left[\cosh\left(\frac{2\sigma_p}{\sigma_c}\right) - \frac{3\sigma_p}{2\sigma_c}\sinh\left(\frac{2\sigma_p}{\sigma_c}\right) + 2\right]R_y, & \text{for bending} \end{cases} \tag{23}$$

## VII. Conclusions

The content of this document provides two new and meaningful criteria for fatigue assessment: 1) energy-based shear fatigue-life-prediction and 2) multi-axial fatigue-life-prediction. Each criterion has been validated through comparison with experimental shear and biaxial fatigue results, respectively. Improvements to the multi-axial life-prediction method can be made by developing a new equivalent stress value that incorporates the nonlinear displacement-load functions used for the energy-based analysis. The new expression will be determined using the distortion-energy theory, which states that yielding begins when energy stored in an element under multi-axial loading is equal to the energy stored in an element under uniaxial loading [21]. Equation (24) is the expression of the distortion-energy theory, where $\sigma_E$ is the new equivalent stress:

$$\frac{2\sigma_c}{C}\left\{\frac{\sigma_E}{\sigma_c}\sinh\left(\frac{2\sigma_E}{\sigma_c}\right) - \left[\cosh\left(\frac{2\sigma_E}{\sigma_c}\right) - 1\right]\right\} = \sum_{p=1}^{3}\frac{2\sigma_c}{C}\left\{\frac{\sigma_p}{\sigma_c}\sinh\left(\frac{2\sigma_p}{\sigma_c}\right) - \left[\cosh\left(\frac{2\sigma_p}{\sigma_c}\right) - 1\right]\right\} \tag{24}$$

Furthermore, since the prediction method introduced in this manuscript is energy-based, it can also be incorporated into a minimal potential energy calculation. This capability is influential, especially to aircraft engine design via FEM software. Most FEM software does not have a fatigue-life-prediction mechanism. Therefore, the development of the energy-based fatigue-life-prediction method for objects under shear and multi-axial loading is also a stepping stone for the advancement of FEM software.

## Acknowledgements

The authors would like to thank the National Research Council and the U.S. Air Force Research Laboratory, specifically, the Turbine Engine Fatigue Facility laboratory, for their financial support, facility and equipment access, and encouragement of this research.

## References


[1] Goodman, J., *Mechanics Applied to Engineering*, Longmans, Green, and Co., London, 1899.

[2] George, T., Seidt, J., Shen, M.-H. H., Cross, C., and Nicholas, T., "Development of a Novel Vibration-Based Fatigue Testing Methodology," *International Journal of Fatigue*, Vol. 26, No. 5, 2004, pp. 477–486. doi:10.1016/j.ijfatigue.2003.10.012

[3] George, T., Seidt, J., Shen, M.-H. H., Cross, C., and Nicholas, T., "Development of a Novel Vibration-Based Fatigue Testing Methodology," *International Journal of Fatigue*, Vol. 26, No. 5, May 2004, pp. 477–486. doi:10.1016/j.ijfatigue.2003.10.012

[4] George, T., Shen, M.-H. H., Scott-Emuakpor, O., Nicholas, T., Cross, C., and Calcaterra, J., "Goodman Diagram via Vibration-Based Fatigue Testing," *Journal of Engineering Materials and Technology*, Vol. 127, No. 1, 2005, pp. 58–64. doi:10.1115/1.1836791

[5] Scott-Emuakpor, O., "Development of an Improved Energy-Based Criterion for Fatigue Life Assessment," M.S., Thesis, The Ohio State Univ., Columbus, OH, 2004.

[6] Jasper, T. M., "The Value of the Energy Relation in the Testing of Ferrous Metals at Varying Ranges of Stress and at Intermediate and High Temperatures," *Philosophical Magazine*, Series 6, Vol. 46, Oct. 1923, pp. 609–627.

[7] Feltner, C. E., and Morrow, J. D., "Microplastic Strain Hysteresis Energy as a Criterion for Fatigue Facture," American Society of Mechanical Engineers, Paper 60-MET-2, 1960.

[8] Enomoto, N., "On Fatigue Tests Under Progressive Stress," *Proceedings*, Vol. 55, American Society for Testing and Materials, West Conshohocken, PA, 1955, p. 903.

[9] Stowell, E., "A Study of the Energy Criterion for Fatigue," *Nuclear Engineering and Design*, Vol. 3, No. 1, 1966, pp. 32–40. doi:10.1016/0029-5493(66)90146-4

[10] Scott-Emuakpor, O., Shen, M.-H. H., Cross, C., Calcaterra, J., and George, T., "Development of an Improved High Cycle Fatigue Criterion," *Journal of Engineering for Gas Turbines and Power*, Vol. 129, No. 1, 2007, pp. 162–169. doi:10.1115/1.2360599

[11] Scott-Emuakpor, O., Shen, M.-H. H., Cross, C., and George, T., "A New Energy-Based Uniaxial Fatigue Life Prediction Method for Commonly Used Gas Turbine Engine Materials," *Journal of Engineering for Gas Turbines and Power*, Vol. 130, No. 6, 2008, Paper 062504. doi:10.1115/1.2943152

[12] Scott-Emuakpor, O., "Development of a Novel Energy-Based Method for Multi-Axial Fatigue Strength Assessment," Ph.D., Dissertation The Ohio State Univ., Columbus, OH, 2007.

[13] Garud, Y. S., "A New Approach to the Evaluation of Fatigue Under Multiaxial Loading," *Journal of Engineering and Material Technology*, American Society of Mechanical Engineers, New York, 1979, pp. 247–264.

[14] "Standard Test Method for Shear Properties of Composite Materials by the *V*-Notched Beam Method," *ASTM Book of Standards*, Vol. 15.03, ASTM International, Standard ASTM D5379M-05, West Conshohocken, PA, 2005.

[15] Nicholas, T., "Critical Issues in High Cycle Fatigue," *International Journal of Fatigue*, Vol. 21, Sept. 1999, pp. 221–231. doi:10.1016/S0142-1123(99)00074-2

[16] George, T., Shen, M.-H. H., Cross, C., and Nicholas, T., "A New Multiaxial Fatigue Testing Method for Variable Amplitude Loading and Stress Ratio," *Journal of Engineering for Gas Turbines and Power*, Vol. 128, No. 4, 2006, pp. 857–864. doi:10.1115/1.1788687

[17] Miyano, T., "High Cycle Fatigue Specimen Topology Design," M.S. Thesis, The Ohio State Univ., Columbus, OH, 2003.

[18] "Strain Gage Rosettes: Selection, Application and Data Reduction," Vishay Micro-Measurements, TN-515, Malvern, PA, 2008.

[19] Sih, G. C., and Jeong, D. Y., "Hysteresis Loops Predicted by Isoenergy Density Theory for Polycrystals, Part 2: Cyclic Heating and Cooling Effects Predicted from Non-Equilibrium Theory for 6061-T6 Aluminum, SAE 4340 Steel and Ti-8Al-1Mo-1V Titanium Cylindrical Bars," *Theoretical and Applied Fracture Mechanics*, Vol. 41, Nos. 1–3, 2004, pp. 267–289. doi:10.1016/j.tafmec.2004.01.001

[20] Nicholas, T., and Maxwell, D., "Mean Stress Effects on the High Cycle Fatigue Limit Stress in Ti-6Al-4V," *Fatigue and Fracture Mechanics*, edited by W. G. Reuter and R. S. Piascik, Vol. 33, STP 1417, ASTM International, West Conshohocken, PA, 2003, pp. 476–492.

[21] Collins, J., *Mechanical Design of Machine Elements and Machines*, Wiley, New York, 2003.


J. Cooper
*Associate Editor*